

# Nuclear star formation in the hot-spot galaxy NGC 2903

A. Alonso-Herrero<sup>1\*</sup>, S. D. Ryder<sup>2</sup> and J. H. Knapen<sup>1,3†</sup>

<sup>1</sup>University of Hertfordshire, Department of Physical Sciences, College Lane, Hatfield, Herts AL10 9AB, UK

<sup>2</sup>Anglo-Australian Observatory, P. O. Box 296, Epping, NSW 1710, Australia

<sup>3</sup>Isaac Newton Group of Telescopes, Apartado 321, E-35700 Santa Cruz de La Palma, Spain

Accepted . Received ; in original form

## ABSTRACT

We present high-resolution near-infrared imaging obtained using adaptive optics and *HST*/NICMOS, and ground-based spectroscopy of the hot-spot galaxy NGC 2903. Our near-infrared resolution imaging enables us to resolve the infrared hot spots into individual young stellar clusters or groups of these. The spatial distribution of the stellar clusters is not coincident with that of the bright H II regions, as revealed by the *HST*/NICMOS Pa $\alpha$  image. Overall, the circumnuclear star formation in NGC 2903 shows a ring-like morphology with an approximate diameter of 625 pc.

The SF properties of the stellar clusters and H II regions have been studied using the photometric and spectroscopic information in conjunction with evolutionary synthesis models. The population of bright stellar clusters shows a very narrow range of ages,  $4 - 7 \times 10^6$  yr after the peak of star formation, or absolute ages  $6.5 - 9.5 \times 10^6$  yr (for the assumed short-duration Gaussian bursts), and luminosities similar to the clusters found in the Antennae interacting galaxy. This population of young stellar clusters accounts for some 7 – 12% of the total stellar mass in the central 625 pc of NGC 2903. The H II regions in the ring of star formation have luminosities close to that of the super-giant H II region 30 Doradus, they are younger than the stellar clusters, and will probably evolve into bright infrared stellar clusters similar to those observed today. We find that the star formation efficiency in the central regions of NGC 2903 is higher than in normal galaxies, approaching the lower end of infrared luminous galaxies.

**Key words:** galaxies: individual: NGC 2903 – infrared: galaxies – galaxies: photometry – galaxies: star clusters – galaxies: starburst

## 1 INTRODUCTION

Numerical simulations of bars have shown that they may provide an efficient mechanism for transporting interstellar gas into the central regions of galaxies. Thus, bars are often invoked as a possible mechanism to fuel nuclear/circumnuclear star formation (SF; Heller & Shlosman 1994), as well as active galactic nuclei (Shlosman, Frank, & Begelman 1989). It is now well established that circumnuclear regions (CNRs) of enhanced SF are commonly associated with the presence of stellar bars (see the recent review by Knapen 1999, and references therein). In particular, a significant percentage of barred galaxies show nuclear rings within 1 kpc from the nucleus of the galaxy; these are be-

lieved to be formed by gas accumulation near galactic resonances. In these nuclear rings, strong density enhancements of gas and increased SF are often observed (Piner, Stone, & Teuben 1995; Knapen et al. 1995b; Buta & Combes 1996; Shlosman 1999).

Knapen (1999) pointed out that CNRs are excellent laboratories for the study of the effects of inflow processes on the triggering of SF. A detailed study of CNRs has been hampered by the lack of imaging at sufficiently high spatial resolution. The main difficulty arises when trying to disentangle the effects of young and old stars, cold gas and dust, and possibly emission from dust heated by the SF activity (e.g. Knapen et al. 1995a, b). High resolution imaging allows one to resolve individual SF sites, to determine their location with respect to dust lanes, and to discover dynamically important morphological features that remain hidden in imaging of CNRs at lower resolution. These features include nested bars (e.g. Knapen et al. 1995a; Phillips et al 1996; Elmegreen et al. 1998; Carollo, Stiavelli, & Mack 1998;

† Visiting Astronomer, Canada–France–Hawaii Telescope operated by the National Research Council of Canada, the Centre National de la Recherche Scientifique de France and the University of Hawaii.

Colina & Wada 2000), leading spiral arms (Knapen et al. 1995a, 2000); nuclear flocculent (e.g., Elmegreen et al. 1999) or even grand-design spirals (Laine et al. 1999).

High resolution near-infrared (NIR) observations of CNR are of particular importance because they are less affected by extinction, and because the NIR emission is a better tracer of old stellar population (and hence of the stellar mass distribution) than optical or ultraviolet observations. However, in sites of strong SF there can be a significant contribution from young red supergiants to the NIR emission, and therefore both NIR spectroscopy and imaging are an absolute need to study the SF processes in CNR (e.g., Engelbracht et al. 1998; Ryder & Knapen 1999; Puxley & Brand 1999; Alonso-Herrero et al. 2000; 2001). Quantifying the contribution of young stars to the NIR emission so the emission from old stars can be isolated is essential for the interpretation of the dynamics of CNRs and of inflow in barred galaxies in general, through the use of dynamical modeling. Such modeling is generally based upon an estimate of the galactic potential as derived from red or NIR imaging, under the assumption of a constant mass-to-light ratio (e.g., Quillen, Frogel, & González 1994; Knapen et al. 1995a). It is important that this assumption be tested, and the circumstances under which the mass-to-light ratio may vary be understood, to allow for more accurate modelling.

In this paper we present high angular resolution NIR adaptive optics (AO) and *HST*/NICMOS imaging, and spectroscopy of the hot-spot galaxy NGC 2903. Although NGC 2903 is classified as an SAB(rs)bc (de Vaucouleurs et al. 1991), the presence of a large scale bar with a position angle (P.A.) of  $\simeq 20$  deg is clearly inferred from *K*-band (Regan & Elmegreen 1997) and  $H\alpha$  (Jackson et al. 1991; Pérez-Ramírez & Knapen 2000) images, as well as from CO observations (Regan, Sheth, & Vogel 1999). Early NIR studies of this galaxy have shown that considerable SF is occurring within the complex hot spot morphology in the nuclear region (e.g., Wynn-Williams & Becklin 1985; Simons et al. 1988). However these studies lacked the necessary spatial resolution to determine whether the SF was confined to these hot spots or not. The infrared luminosity ( $8 - 1000 \mu\text{m}$ ) of NGC 2903 is  $9.1 \times 10^9 L_{\odot}$  (Sakamoto et al. 1999) which is similar to (although slightly smaller than) those of M82 and NGC 253, both also well known hot-spot galaxies. Throughout the paper we will assume a distance to NGC 2903 of  $d = 8.6$  Mpc (Telesco & Harper 1980), for which  $1 \text{ arcsec} \simeq 42 \text{ pc}$ . This paper is organized as follows. Section 2 describes the observations. Section 3 discusses the morphology, and Section 4 the extinction. The properties of the stellar clusters and H II regions are studied in Sections 5 and 6, while conclusions are given in Section 7.

## 2 OBSERVATIONS

### 2.1 CFHT AO *K'*-band imaging

We obtained a *K'*-band image of the central region of NGC 2903 on 1998 October 25 with the Canada France Hawaii Telescope (CFHT), equipped with the adaptive optics (AO) system PUEO (Rigaut et al. 1999) and the KIR camera, a high resolution  $1024 \times 1024$  NIR camera based on a Rockwell HAWAII HgCdTe array. PUEO uses a curvature mirror and a wavefront sensor to give, under favourable

circumstances, diffraction limited images at *H* and *K*. We used the nucleus of the galaxy itself as the AO guide source, which is not a point source and thus does not allow PUEO to reach this full correction. We estimate that the natural seeing of around  $0.6 \text{ arcsec}$  at the time of the observations was improved to a resolution in the final image of about  $0.25 \text{ arcsec}$ . The total integration time was 240 seconds, made up from 4 individual dithered exposures. The individual images were sky-subtracted, flatfielded, corrected for bad pixels and combined into the final mosaic. KIR's image scale is  $0.03438 \pm 0.0007 \text{ arcsec pixel}^{-1}$ , and the total field of view of the individual exposures is  $36 \text{ arcsec} \times 36 \text{ arcsec}$ . As the nucleus of the galaxy was positioned at various locations across the array during individual exposures, the total field of view of the final images is slightly larger ( $46 \text{ arcsec} \times 46 \text{ arcsec}$ ). The fully reduced image is presented in the left panel of Figure 1.

Flux calibration of the image was performed by observing standard stars from the list of Hawarden et al. (2000). The uncertainty in the photometric calibration of the image is about  $0.05 \text{ mag}$ .

### 2.2 *HST*/NICMOS observations

We obtained NIR observations of NGC 2903 from the *HST* archive. The images were taken with camera NIC2 (pixel size  $0.076 \text{ arcsec pixel}^{-1}$ ) through the F160W filter (equivalent to a ground-based *H*-band filter), and with camera NIC3 (pixel size  $0.2 \text{ arcsec pixel}^{-1}$ ) taken through filters F160W and F187N (the latter filter contains the emission line  $\text{Pa}\alpha$  and continuum at  $1.87 \mu\text{m}$ ). The NIC3 observations are part of the survey of nearby galaxies conducted by Böker et al. (1999).

Standard data reduction procedures were applied (see Alonso-Herrero et al. 2000 for more details). The reduced NICMOS images were rotated to the usual orientation (north up, east to the left). The spatial resolutions (FWHM) of the NIC2 and NIC3 images are  $0.15 \text{ arcsec}$  ( $6 \text{ pc}$ ) and  $0.3 \text{ arcsec}$ , respectively, as measured from unresolved sources in the images. These sources show diffraction rings so we can be certain that good estimates of the resolution can be obtained from them. The flux calibration was performed using the conversion factors based on measurements of the standard star P330-E taken during the Servicing Mission Observatory Verification (SMOV) programme (M.J. Rieke 1999, private communication). Unfortunately there are no observations available of the adjacent continuum to  $\text{Pa}\alpha$ , so we used the flux calibrated continuum image at  $1.6 \mu\text{m}$ . Ideally continuum images on both sides of the emission line are needed to perform an accurate continuum subtraction which takes into account the spatial distribution of the extinction. However, the continuum subtracted  $\text{Pa}\alpha$  image (flux calibrated) does not show negative values suggesting that the continuum subtraction was relatively accurate and that the differential extinction between  $1.60 \mu\text{m}$  and  $1.87 \mu\text{m}$  does not play a dominant role. The continuum subtracted  $\text{Pa}\alpha$  image is presented in the right panel of Figure 1.

An *H* - *K'* colour map was constructed using the *HST*/NICMOS *H*-band and the AO *K'*-band images. The process involved rebinning of the *K'*-band image to the same pixel size as the NICMOS image and smoothing of the NICMOS image to match the effective resolution of the AO im-

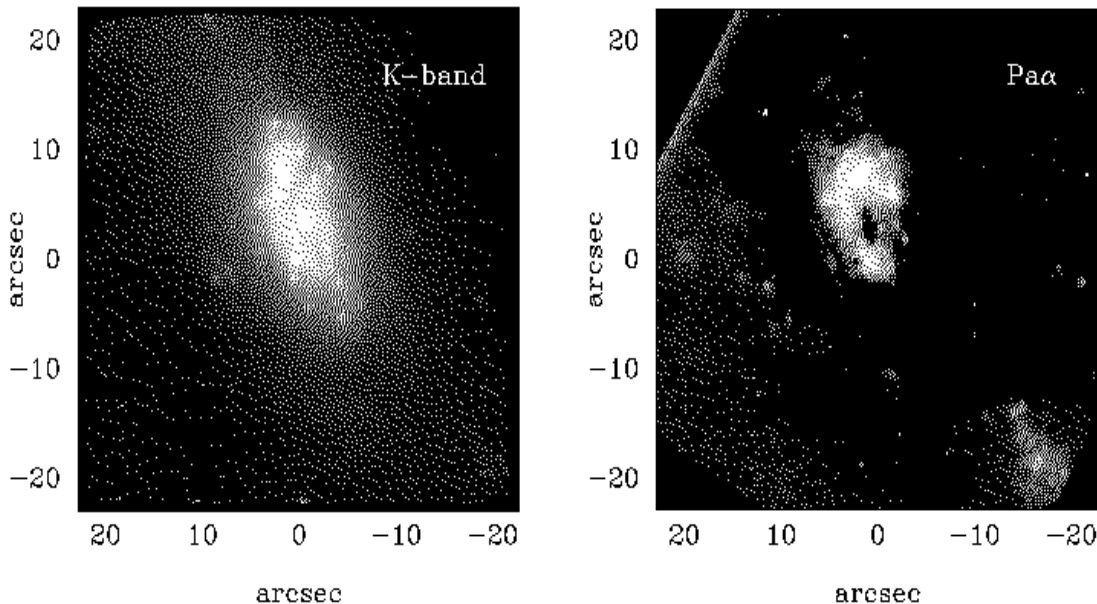


**Figure 1.** *Left panel:* CFHT/PUEO AO  $K'$ -band image. *Right panel:* Continuum-subtracted  $\text{Pa}\alpha$  (NIC3 F187N) image. Both images are displayed on a logarithmic scale. The field of view is  $46 \text{ arcsec} \times 46 \text{ arcsec}$  and the orientation is north up, east to the left.

age. The  $H - K'$  colour map along with the NIC2 F160W image are presented in Figure 2.

### 2.3 NIR Spectroscopy

Long-slit spectroscopy of the central regions of NGC 2903 was carried out on 1998 December 25–26 UT, and on 1999 April 1 UT, using the common-user NIR spectrograph CGS4 (Mountain et al. 1990) on the United Kingdom Infrared Telescope (UKIRT) at Mauna Kea. The observing setup was essentially identical to that of Ryder, Knapen & Takamiya (2000), viz. a  $1.2 \text{ arcsec}$  slit,  $0.61 \text{ arcsec pixel}^{-1}$ , and a  $40 \text{ line mm}^{-1}$  grating in first order, yielding complete spectral coverage between  $1.85$  and  $2.45 \mu\text{m}$  at an effective resolving power  $R \sim 450$ . Using the AO  $K'$ -image (Figure 1, left panel), a total of five slit position angles and nuclear offsets were selected, as marked on Figure 3 (see also Table 1); four of these cover at least 3 stellar clusters each, while the fifth samples the background stellar continuum.

After setting the image rotator to the desired slit position angle, a manual search for the  $K$ -band nuclear peak was conducted, following which accurate offsets were applied by use of the UKIRT crosshead to place the slit at exactly the positions marked on Figure 3. During observations, the detector array was micro-stepped by half a resolution element every 30 seconds, to sub-sample the spectra and to com-

pen-  
 pensate for bad pixels; after four such steps, the telescope itself was nodded by  $36.6 \text{ arcseconds}$  along the slit to collect the sky spectrum, while recording the object spectra on the opposite half of the detector. These object-sky exposure pairs were differenced, and the result co-added until the total on-source integration times listed in Table 1 were achieved. All observations of NGC 2903 were bracketed by observations of the A2 V star BS 3657 at a similar airmass, to assist with removal of some of the telluric features.

Data reduction has been carried out using a combination of tasks within the Starlink CGS4DR and NOAO IRAF<sup>‡</sup> packages. After flatfielding of the co-added object-sky pairs, any residual sky lines were removed by fitting a low-order polynomial to each row of the spatial axis. Plots of the variation of continuum emission along the slit were compared with the AO  $K'$ -band image to define extraction apertures appropriate to each cluster. In several cases it proved impossible, at the  $0.61 \text{ arcsec pixel}^{-1}$  scale of CGS4, to separate the spectra of neighboring clusters, so the net emission from both was extracted. After extraction, the spectra were wavelength-calibrated using observations of an Argon arc

<sup>‡</sup> IRAF is distributed by the National Optical Astronomy Observatories, which are operated by the Association of Universities for Research in Astronomy, Inc., under cooperative agreement with the National Science Foundation.

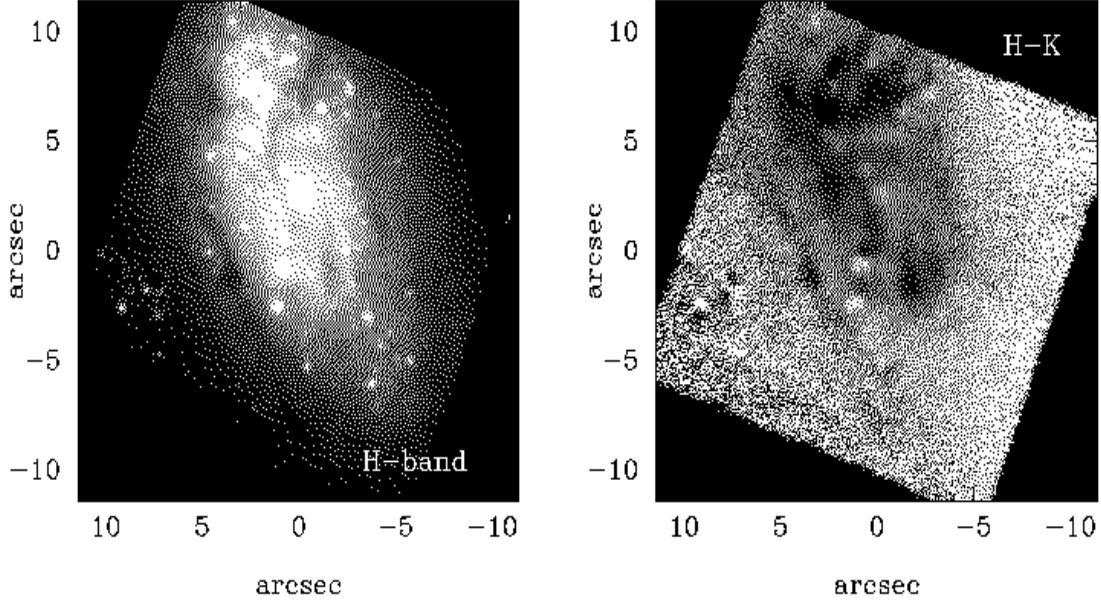


**Figure 2.** *Left panel:* H-band (NIC2 F160W) image displayed on a logarithmic scale. *Right panel:*  $m_{F160W} - K'$  (equivalent to a ground-based  $H - K'$ ) colour map. Dark colours indicate regions with high extinction. The  $m_{F160W} - K'$  colour map is displayed from 0.1 to 0.8 mag. The field of view of both images is 22 arcsec  $\times$  22 arcsec.

lamp. The strong  $\text{Br}\gamma$  absorption intrinsic to BS 3657 was interpolated over, prior to dividing its spectrum into that of each of the clusters, and scaling by a blackbody curve corresponding to the temperature (8810 K) and flux density ( $K = 6.46$ ) of BS 3657. Figure 4 shows the fully reduced spectra of clusters 2+3 (in slit 4) and the W position (in slit 5).

To define an objective continuum level right across the region of extensive CO absorption redward of  $2.3 \mu\text{m}$ , we fitted a power-law of the form  $F_\lambda \propto \lambda^\beta$  to featureless sections of the cluster spectra near  $2.11$  and  $2.27 \mu\text{m}$  (rest wavelength), and normalised by this fit. The equivalent width (EW) of the  $\text{Br}\gamma$  emission line was determined by fitting a Gaussian to the profile using the *splot* task in IRAF. The CO spectroscopic index, as defined by Doyon, Joseph, & Wright (1994) has also been measured:

$$\text{CO}_{\text{sp}} = -2.5 \log \langle R_{2.36} \rangle \quad (1)$$

where  $R_{2.36}$  is the mean normalised intensity between  $2.31$  and  $2.40 \mu\text{m}$  in the rest frame of the galaxy (for NGC 2903, this corresponds to the wavelength interval  $2.314 - 2.404 \mu\text{m}$ ). At the (comparatively low) resolution of these observations, this measure of the CO absorption due to young supergiants was found by Ryder et al. (2000) to be more reliable than the narrower interval favoured by Puxley,

Doyon, & Ward (1997). The equivalent photometric CO index has then been computed using the transformation given by Doyon et al. (1994):

$$\text{CO}_{\text{ph}} = (\text{CO}_{\text{sp}} + 0.02)/1.46 \quad (2)$$

for direct comparison with the evolutionary synthesis models (Section 5.2). In Table 2 we give the EW of  $\text{Br}\gamma$  and photometric and spectroscopic values of the CO index and their corresponding errors sorted by the slit number. In cases where the same cluster(s) were observed by different slits, we find extremely good agreements (e.g., the nucleus in slits 1 and 3, and clusters 2+3 in slits 3 and 4). The one exception is clusters 1+9 in slits 1 and 4, but as can be seen from Figure 3, there is less flux from cluster 9 in slit 4. The slit 5 regions E and W ( $7.3 \text{ arcsec}$  E and W of the nucleus as shown in Figure 3) have only upper limits on  $\text{Br}\gamma$ , but are included to indicate the intrinsic CO index of the underlying population.

### 3 MORPHOLOGY

Figure 1 presents the CFHT/PUEO AO  $K'$ -band image and the *HST*/NICMOS continuum-subtracted Pa $\alpha$  image of the central 46 arcsec ( $\simeq 2 \text{ kpc}$ ) of NGC 2903. The continuum

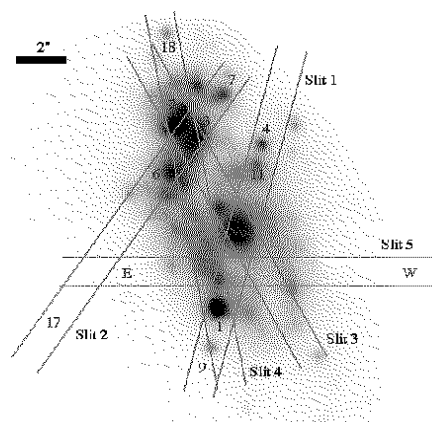


**Figure 3.** Location of the CGS4 slit positions observed, together with identifications of the stellar clusters extracted, marked on the AO  $K'$ -band image. The numbers refer to the cluster ID in Tables 2 and 3, except for clusters 17 and 18 (which are outside the field of the *HST*/NICMOS image), and the positions marked "E" and "W" along Slit 5, which do not correspond to any particular cluster but instead sample the background stellar continuum.

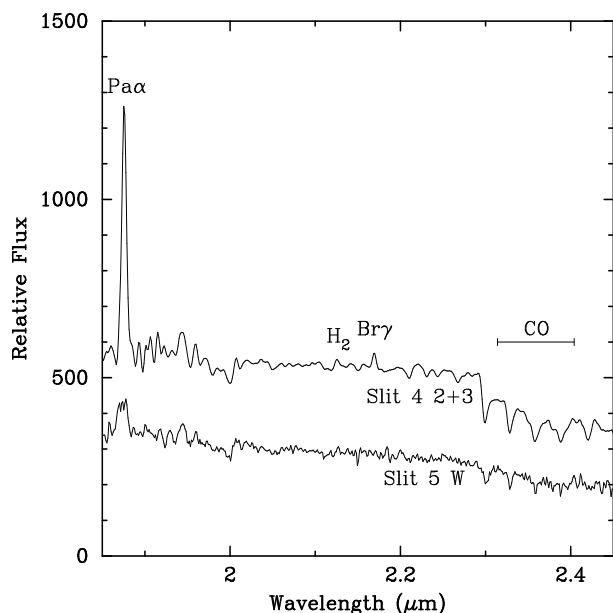


**Figure 4.** NIR spectra of clusters 2 + 3 from Slit 4 (top), and background stellar continuum from W position of Slit 5 (see Figure 3 and Table 1). The locations of the prominent emission features, as well as the extent of the CO band, are marked. The features between 1.9 and 2.0  $\mu\text{m}$  are nearly all telluric and standard star residuals.

**Table 1.** CGS4 Slit Parameters for NGC 2903.

Slit	P.A.	Clusters	$t_{\text{exp}}$
1	165.6	1,4,(nucleus),9,11	5760
2	148.9	3,6,7,16	5760
3	26.0	2,3,(nucleus)	5760
4	11.9	1,2,3,17	4560
5	90.0	none	9000

Notes.— See Table 3 for identification of continuum knots. Cluster number 16 is near the edge of  $H$ -band image and cluster 17 is too faint, and are not included in the photometry of Table 3.

**Table 2.** Spectroscopy of the nucleus and bright stellar clusters in NGC 2903.

Cluster(s)	EW( $\text{Br}\gamma$ ) ( $\text{\AA}$ )	$\text{CO}_{\text{sp}}$	$\text{CO}_{\text{ph}}$
<b>Slit 1</b>			
1+9	$2.4 \pm 0.2$	$0.27 \pm 0.01$	$0.20 \pm 0.01$
nucleus	$2.3 \pm 0.8$	$0.22 \pm 0.01$	$0.16 \pm 0.01$
4+11	$8.7 \pm 0.4$	$0.21 \pm 0.01$	$0.16 \pm 0.01$
<b>Slit 2</b>			
6	$4.6 \pm 0.3$	$0.25 \pm 0.01$	$0.18 \pm 0.01$
3	$2.1 \pm 0.7$	$0.32 \pm 0.01$	$0.23 \pm 0.01$
7	$3.5 \pm 0.5$	$0.28 \pm 0.01$	$0.21 \pm 0.01$
17	$< 1.9$	$0.26 \pm 0.02$	$0.19 \pm 0.02$
<b>Slit 3</b>			
nucleus	$2.5 \pm 0.2$	$0.22 \pm 0.01$	$0.16 \pm 0.01$
2+3	$4.7 \pm 0.3$	$0.30 \pm 0.01$	$0.22 \pm 0.01$
<b>Slit 4</b>			
1+9	$3.8 \pm 0.2$	$0.27 \pm 0.01$	$0.20 \pm 0.01$
2+3	$4.7 \pm 0.2$	$0.30 \pm 0.01$	$0.22 \pm 0.01$
18	$1.7 \pm 0.3$	$0.26 \pm 0.02$	$0.19 \pm 0.02$
<b>Slit 5</b>			
E	$< 1.1$	$0.21 \pm 0.02$	$0.16 \pm 0.02$
W	$< 3.2$	$0.20 \pm 0.02$	$0.15 \pm 0.02$

light (see also Figure 2, left panel for a close-up of the  $H$ -band emission) resolves the already known infrared hot spots (e.g., Wynn-Williams & Becklin 1985; Simons et al. 1988; Pérez-Ramírez et al. 2000) into a large number of individual stellar clusters.

The most striking feature of the emission in NGC 2903 is the lack of spatial correspondence between the bright  $\text{H II}$  regions seen in the  $\text{Pa}\alpha$  image and the position of the stellar clusters (see superposition of the  $\text{Pa}\alpha$  emission on the  $H$ -band emission in Figure 5). Previous works of this galaxy at lower spatial resolution identified the bright infrared hot spots with sites of intense SF (e.g., Wynn-Williams & Becklin 1985). It now appears that the bright NIR sources although close to the  $\text{H II}$  regions, are not coincident with them. Other high resolution NIR studies of star forming galaxies have found a similar result and interpret the bright infrared stellar clusters as the result of the evolution of giant  $\text{H II}$  regions (see for instance, Alonso-Herrero et al. 2000,

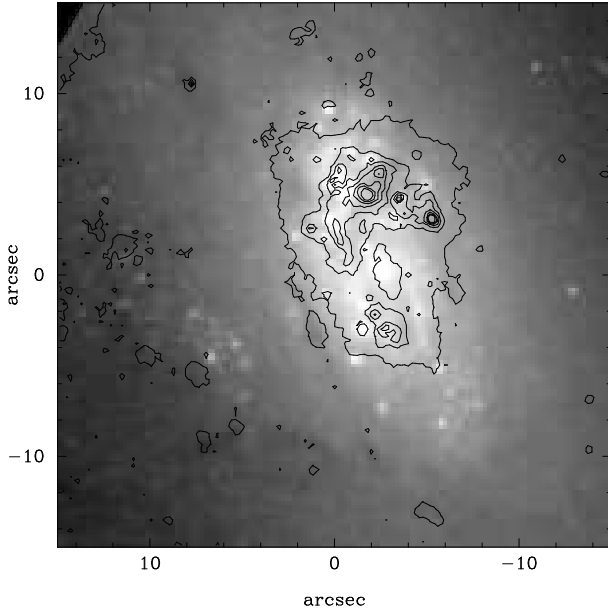


**Figure 5.** *H*-band (NIC3 F160W) continuum image (grey scale) on a logarithmic scale and, superimposed, the continuum subtracted Pa $\alpha$  image (black contours on a linear scale).

2001). The properties of the stellar clusters and the H II regions in NGC 2903 are discussed in Sections 5 and 6.

The *HST*/NICMOS Pa $\alpha$  line emission map reveals, for the first time, the presence of a nuclear ring-like morphology with an apparent diameter of approximately 15 arcsec = 625 pc. The ring is composed of a number of bright individual H II regions embedded in a diffuse component. Thanks to the reduced extinction in the NIR, this ring shows up more prominently in Pa $\alpha$  than in H $\alpha$  observations of the nuclear region of NGC 2903 (see for instance Planesas, Colina, & Pérez-Olea 1997). The southern part of the ring is fainter than the northern part; the *H* – *K'* colour map shows that this is not an extinction artifact.

The right panel of Figure 2 shows the  $m_{F160W} - K'$  (equivalent to a ground-based *H* – *K'*) colour map constructed with the *H*-band *HST*/NICMOS image and the AO *K'*-band images. Colour maps with a larger field of view can be found in Pérez-Ramírez et al. (2000). The *H* – *K'* colour map (which is assumed to trace mainly the extinction to the stars) reveals the complex morphology of the obscuration in the centre of this galaxy. The bright stellar clusters may appear artificially bluer due to the different point spread functions of the AO and NICMOS images. The extinction appears to be higher in regions to the north of the nucleus, where the Pa $\alpha$  emission is also brighter, ruling out the possibility that extinction is hiding the Pa $\alpha$  emission from the southern part of the ring of SF. This asymmetric distribution of the dust in the central regions of NGC 2903 was already noticed from lower spatial resolution studies involving optical and NIR imaging (Simons et al. 1988).

The asymmetry seen in the H II region and obscuration distributions is also apparent in the distribution of the bright stellar clusters, whose number is more elevated to the north of the centre of NGC 2903. On large scales, both the gas and continuum emissions appear very symmetric (see e.g. the *K*-band image in Regan & Elmegreen 1997; the H $\alpha$  image in

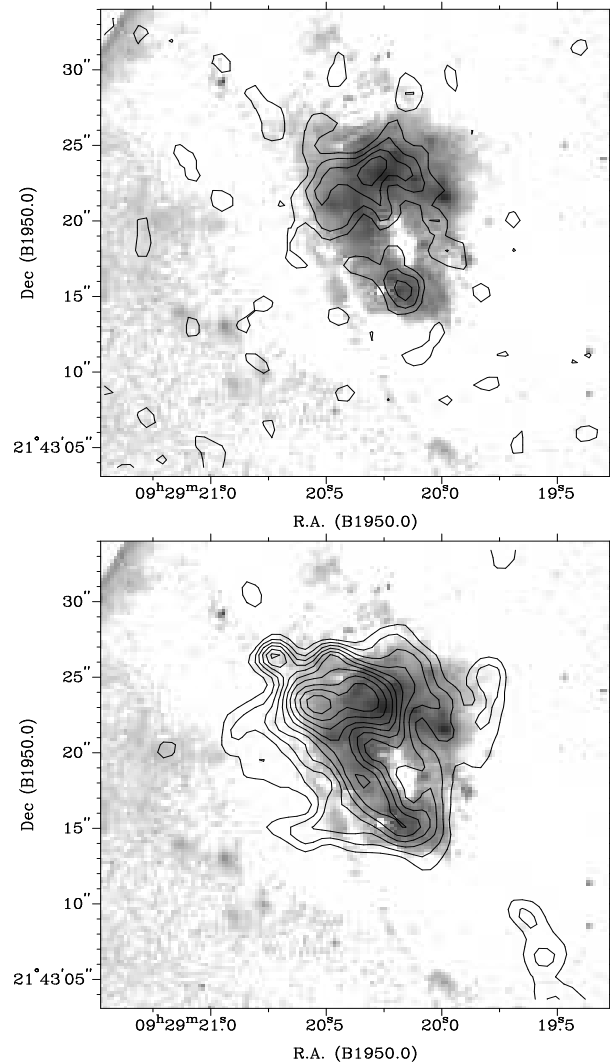


**Figure 6.** *Upper panel:* Continuum subtracted Pa $\alpha$  (grey scale) on a logarithmic scale and 2 cm radio map (black contours) on a linear scale from Wynn-Williams & Becklin (1985). *Lower panel:* as in upper panel but the contours are the 20 cm radio map. The resolution of the radio maps is approximately 2 arcsec (FWHM).

Jackson et al. 1991; and the optical broad-band and H $\alpha$  images in Pérez-Ramírez & Knapen 2000).

Another puzzling result from previous NIR studies of this galaxy was the lack of spatial correspondence between the optical and 2.2  $\mu$ m continuum morphologies and the radio emission (Wynn-Williams & Becklin 1985; Simons et al. 1988). However when we superimpose the radio emission maps (at 2 cm and 20 cm) from Wynn-Williams & Becklin (1985) on the *HST*/NICMOS Pa $\alpha$  image for which we used the astrometry information as given in the headers of the image data files) we find an excellent overall correspondence between the line emission and the radio morphologies (Figure 6), as did Planesas et al. (1997). The north and south peaks detected in the 2 cm radio image (Wynn-Williams & Becklin 1985) are clearly identified with H II region emission in the ring of SF. This is in good agreement with the result that a significant fraction of the radio emission in this galaxy is thermal in origin (free-free emission from H II

regions, Wynn-Williams & Becklin 1985). Additional support comes from the radio spectral indices of the north and south peaks detected in the radio maps (Wynn-Williams & Becklin 1985), and from the good agreement between predicted free-free emission at 2 cm from the number of ionizing photons (Simons et al. 1988) and the observed flux densities. The lack of a detailed correspondence level of the individual emitting regions is probably a resolution effect, since the resolution of the radio map is an order of magnitude poorer than that of the *HST*/NIRC2 map.

#### 4 EXTINCTION

In Figure 2 (right panel) we show an  $H - K'$  colour map which traces the extinction to the stars. An advantage of using a NIR colour map to derive the extinction is that the NIR colours do not depend on the age of the population as strongly as optical colours (see Section 3.1). Assuming a colour of the unreddened stellar population of  $H - K' = 0.2$  and a simple foreground dust screen model, we find values of the visual extinction to the stars of  $A_V = 9.5$  mag using Rieke & Lebofsky's (1985) extinction law. The average value of the extinction over the entire view of the colour map is  $A_V = 2.3$  mag, equivalent to an extinction in the  $H$ -band of  $A_H = 0.4$  mag. In Table 3 we give the  $m_{F160W} - K'$  colour (equivalent to a ground-based  $H - K'$  colour) of the nucleus of NGC 2903. In a similar fashion as above we derived an extinction to the nucleus of NGC 2903 of  $A_V = 3.8$  mag, which is relatively modest compared with the higher values found to the north of the nucleus where most of the SF is occurring.

Beck et al. (1984) derived a value of the visual extinction to the gas within the central 8 arcsec of  $A_V = 7$  mag from the NIR hydrogen recombination lines  $Br\gamma$  and  $Br\alpha$ . We made use of these line measurements and our  $P\alpha$  line flux measured through the same aperture, and Rieke & Lebofsky (1985) extinction law. The intrinsic values of the line ratios (for case B recombination) were taken from Hummer & Storey (1987) for the assumed physical conditions of the gas  $T_e = 10^4$  K and  $n_e = 100$  cm $^{-2}$ . We derive values for the visual extinction of  $A_V = 7.0 \pm 2.5$  mag from  $P\alpha/Br\gamma$ ,  $A_V = 5.8 \pm 0.9$  mag from  $P\alpha/Br\alpha$ , and  $A_V = 5.1 \pm 1.5$  mag from  $Br\alpha/Br\gamma$ . The errors in the extinction take into account a 10% uncertainty in the  $P\alpha$  flux calibration. All the values of the extinction to the gas are consistent to within the observational errors, and are in relatively good agreement with the average value of the extinction to the stars over the same region from the  $H - K'$  colour map ( $A_V \simeq 3$  mag).

We can carry out a more detailed study of the spatial distribution of the extinction to the gas at the location of the individual H II regions using our  $P\alpha$  image and the  $H\alpha$  fluxes given by Planesas et al. (1997). We have identified 8 bright H II regions in the  $P\alpha$  image (see Figure 7 and Table 4). A careful cross-correlation between the positions of these H II regions seen in the  $P\alpha$  image (see Table 4 for relative positions with respect to the peak of continuum emission) and those identified by Planesas et al. (1997) from their  $H\alpha$  image shows that there are six correspondences (see Table 4). We used the 2 arcsec-diameter (circular aperture)  $H\alpha$  fluxes from Planesas et al. (1997) and  $P\alpha$  line flux

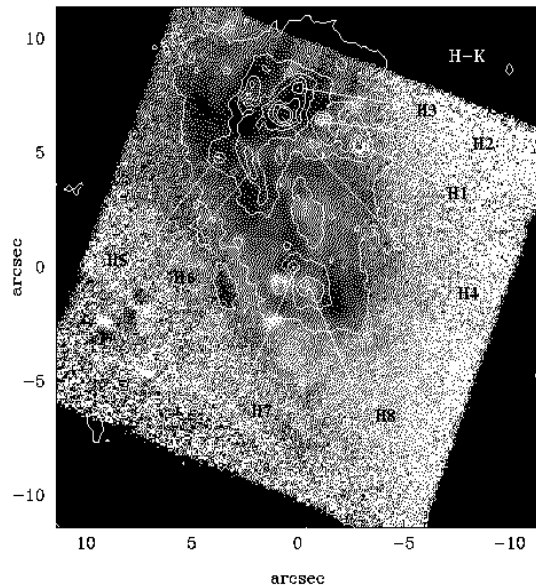


**Figure 7.**  $H - K'$  colour map (grey scale, as in Figure 2) with the continuum subtracted  $P\alpha$  image (white contours) superimposed on a linear scale. The names of the brightest H II regions are indicated (see Table 4).

measurements for the H II regions seen in both images (thus, relatively low extinction regions). Again a simple foreground dust screen model is assumed for the geometry of the gas. We list the values of the visual extinction and the corresponding errors in Table 4; these are between  $A_V = 1.8$  mag and  $A_V = 3.8$  mag using a foreground dust screen model. The errors of the extinction were computed assuming a 10% uncertainty in the  $P\alpha$  fluxes. The fact that regions H5 and H7 are not seen in the  $H\alpha$  image is probably indicating that the extinction to these regions is elevated. The foreground dust screen model always gives a lower limit to the extinction. In a more realistic model with a uniform distribution of stars mixed homogeneously with dust, the derived values of the visual extinctions are between  $A_V = 5$  and  $A_V = 15$  mag for the sources in Table 4 (except for source H4).

The values of the extinction to the gas of the H II regions are slightly smaller than the corresponding values of the extinction to the stars at the same positions as derived from the  $H - K'$  colour map, although the relative values seem to be in good agreement (when the foreground dust screen model is used). For instance from Figure 7 it is clear that H4 lies in a region with higher extinction than H1 or H2. Regions H5 and H7 (which are not detected in the optical) are faint and are located close to regions of high extinction. The discrepancies between the extinction values obtained from the  $H - K'$  colour map and the hydrogen recombination lines involving  $H\alpha$  are most likely due to the simplistic assumption for the dust geometry as well as to optical depth effects in the regions with higher extinction. Using  $H\alpha$  fluxes will bias the extinction calculations towards the outer regions which are dominated by lower obscuration (see discussion in Alonso-Herrero et al. 2000). Summarizing, although the

**Table 3.** Photometry of the nucleus of NGC 2903 and bright stellar clusters.

Source	x off (arcsec)	y off (arcsec)	$m(\text{F160W})$	$K'$	$m_{\text{F160W}} - K'$	$M_{\text{F160W}}$
Nucleus	0.	0.	12.99	12.55	0.44	-16.68
1	+0.9	-3.4	14.64	14.46	0.18	-15.03
2	+2.6	+4.8	15.04	14.61	0.43	-14.62
3	+2.0	+3.9	15.75	15.45	0.30	-13.92
4	-1.1	+4.0	15.76	15.54	0.22	-13.92
5	+1.8	+4.3	15.77	15.41	0.36	-13.90
6	+2.9	+2.6	15.77	15.55	0.22	-13.90
7	+0.6	+6.2	15.82	15.65	0.17	-13.85
8	+0.8	+1.0	15.90	15.71	0.19	-13.75
9	+1.1	-5.2	16.00	15.87	0.13	-13.67
10	+2.3	+5.4	16.26	15.26	1.00	-13.41
11	-0.8	+3.0	16.46	16.41	0.05	-13.21
12	-2.3	-2.6	16.48	15.97	0.51	-13.19
13	-3.5	-5.6	16.52	16.33	0.19	-13.15
14	+1.7	+6.5	16.57	16.49	0.08	-13.10
15	+3.1	+1.7	16.63	16.19	0.44	-13.04

Notes.— The photometry of the nucleus is through a 1.4 arcsec-diameter aperture, whereas the photometry of the stellar clusters is through a 0.8 arcsec-diameter aperture. The absolute F160W ( $H$ -band) magnitudes are not corrected for extinction.

**Table 4.** Photometry of the bright H II regions in the ring of SF.

Source	x off (arcsec)	y off (arcsec)	$f(\text{Pa}\alpha)$ ( $\text{erg cm}^{-2} \text{s}^{-1}$ )	$A_V$ (mag)	$\log L(\text{H}\alpha)$ ( $\text{erg s}^{-1}$ )	$\log N_{\text{Ly}}$ ( $\text{s}^{-1}$ )	optical counterpart
H1	-2.8	+2.8	$2.06 \times 10^{-14}$	$1.8 \pm 0.4$	39.31	51.18	R2
H2	-1.0	+3.8	$1.49 \times 10^{-14}$	$1.8 \pm 0.4$	39.17	51.03	R1
H3	0.0	+5.4	$2.13 \times 10^{-14}$	$2.7 \pm 0.4$	39.37	51.23	R8
H4	+0.7	+4.1	$3.32 \times 10^{-14}$	$3.8 \pm 0.4$	39.63	51.50	R7
H5	+3.6	+2.2	$1.04 \times 10^{-14}$	–	38.90	50.77	–
H6	+2.4	+2.4	$1.62 \times 10^{-14}$	$1.8 \pm 0.4$	39.20	51.07	R6
H7	+0.4	-2.6	$0.94 \times 10^{-14}$	–	38.86	50.72	–
H8	-0.4	-3.2	$1.31 \times 10^{-14}$	$2.2 \pm 0.4$	39.13	51.00	R4
ring	–	–	$5.28 \times 10^{-13}$	$5.8 \pm 0.9$	40.95	52.82	–

Notes.— Columns (2) and (3) Offsets with respect to the nucleus of NGC 2903 (peak of continuum emission). Column (4) Observed Pa $\alpha$  flux through a 1.2''-diameter aperture (50 pc). Column (5) Visual extinction to the gas as derived from the observed Pa $\alpha$  to H $\alpha$  line ratios using a foreground dust screen model. Column (6) H $\alpha$  luminosities (corrected for extinction when available). Column (7) Number of ionizing photons. Column (8) Correspondence with the H $\alpha$  sources detected in Planesas et al. (1997). The total ring Pa $\alpha$  flux and H $\alpha$  luminosity (the latter corrected for extinction) correspond to a 14 arcsec-diameter aperture.

distribution of the obscuring material in the central regions of NGC 2903 is quite complex, the values found for the extinction in the NIR are relatively modest, and therefore for the analysis in the next two sections we will assume that the extinction does not play a relevant role.

## 5 THE YOUNG STELLAR CLUSTERS

Recent high resolution *HST* and ground-based studies have shown growing evidence for a conspicuous presence of young stellar clusters in a variety of galactic environments: interacting galaxies (the Antennae galaxy, Whitmore et al. 1999

and references therein), galaxies with CNR (Barth et al. 1995; Ryder & Knapen 1999), infrared luminous and ultra-luminous galaxies (Surace et al. 1998; Alonso-Herrero et al. 2000, 2001; Scoville et al. 2000).

The properties, nature and evolution of these young stellar clusters are relevant for the understanding of the processes triggering the SF in such diverse environments. In what follows we will study in detail the properties of the stellar clusters in NGC 2903 making use of both the spectroscopic and imaging information.



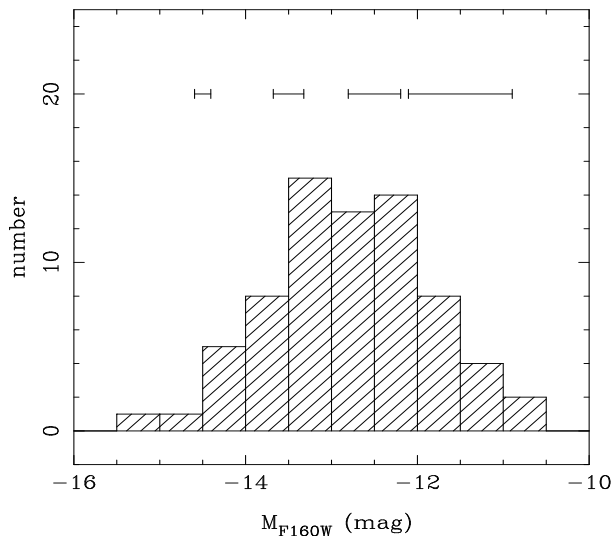


**Figure 8.** Histogram of the absolute  $H$ -band (NIC2 F160W) magnitudes of the brightest stellar clusters in the central region of NGC 2903. The errors are average values per magnitude interval.

### 5.1 Luminosities

We used *daophot* within IRAF to identify stellar clusters on the NIC2 F160W image (which is the image with the highest angular resolution). We found 71 individual clusters in the central 20 arcsec (830 pc) of NGC 2903. From the larger field of view of the NICMOS (NIC3) and AO images, it is apparent that most of the bright stellar clusters are confined within the nuclear region, and thus they are representative of the population of bright stellar clusters. We performed aperture photometry through a 0.61 arcsec-diameter (corrected for aperture effects, M. Rieke 1999, private communication). The surrounding (underlying) galaxy emission was subtracted using the mean background value from within an annulus from 1.0 arcsec and 1.4 arcsec around each source.

Figure 8 shows a histogram of the absolute F160W magnitudes (equivalent to ground based absolute  $H$ -band magnitudes) for the brightest 71 clusters in the central region of NGC 2903, using a distance modulus of  $m - M = 29.67$ . The absolute magnitudes have not been corrected for extinction. The effect of this correction would be small since the average extinction in the  $H$ -band is relatively small ( $A_H = 0.4$  mag) if the foreground dust screen model is used. The average absolute magnitude is  $M_H = -13$  mag. The errors per magnitude interval were computed assuming a typical error of 10% associated with the galaxy background subtraction. In Figure 8 we show the average value of the error per magnitude interval. The actual value for a given cluster depends on the brightnesses of both the source and the local background. Our cluster detection is not complete, and we anticipate that most of the faint stellar clusters have been missed. The detection efficiency varies with the brightness of the source, local galaxy background and crowding.

The luminosities of the stellar clusters detected in NGC 2903 are similar to those in M100 (Ryder & Knapen 1999) or NGC 1097 (Barth et al. 1995), both are barred galaxies which contain bright hot spots as in NGC 2903. Moreover, the luminosities of the stellar clusters in NGC 2903 are comparable to those of the bright-

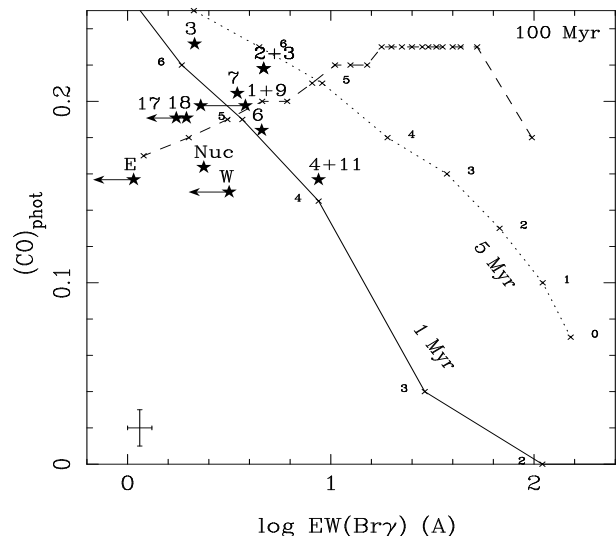


**Figure 9.** Photometric CO index versus EW of  $\text{Br}\gamma$ . The lines are models (Rieke et al. 1993) with a Gaussian burst with the FWHM indicated next to the curves. The crosses on the 1 Myr and 5 Myr curves are the ages after the peak of SF indicated by the small numbers next to them. The filled stars are the measurements for the stellar clusters (Table 2). The typical error bars of our measurements are plotted in the bottom left corner. The arrows indicate an upper limit on the EW of  $\text{Br}\gamma$ . The two values of the EW of  $\text{Br}\gamma$  for 1+9 (Table 3) are connected with a line.

est (young) stellar clusters found in the interacting galaxy The Antennae (Whitmore et al. 1999) which range from  $M_H = -13.3$  mag up to  $M_H = -15.9$  mag (assuming a typical colour of  $V - H \simeq 2$ ), although fainter than those detected in the infrared interacting galaxies Arp 299 and NGC 1614 (Alonso-Herrero et al. 2000, 2001).

Some of the clusters are unresolved, but the typical size of 8 pc (FWHM) is in good agreement with the sizes measured for the stellar clusters in the Antennae galaxy ( $R_{\text{eff}} = 0 - 10$  pc, Whitmore et al. 1999).

### 5.2 Ages

The spectroscopic information of the bright stellar clusters (EW of  $\text{Br}\gamma$  and the values of the CO index) is a valuable tool to constrain their ages. The EWs of hydrogen recombination lines are a good measure of the age of the starburst since the luminosity of the lines is directly proportional to the number of ionizing photons. In particular, the EW of  $\text{Br}\gamma$  measures the number of young stars (producing the ionizing photons) relative to the number of red supergiants. The strength of the  $2.29 \mu\text{m}$  CO band is sensitive to the stellar effective temperature and surface gravity and it is often used to determine the existence of red supergiants. Thus a diagram of the CO index versus the EW of  $\text{Br}\gamma$  can be used to constrain in detail the ages of the SF episodes (e.g., Puxley et al. 1997; Vanzi, Alonso-Herrero, & Rieke 1998; Ryder & Knapen 1999).

We use Rieke et al. (1993) models with a single burst of SF with Gaussian FWHM values of 1 Myr, 5 Myr and 100 Myr. The longest Gaussian burst represents a slowly evolving population with quasi constant SF. For the IMF slope we chose a Salpeter form with lower and upper mass

cutoffs of 1 and  $80 M_{\odot}$  respectively. The outputs from the models together with the observations of the brightest stellar clusters are shown in Figure 9. The numbers on the 1 Myr and 5 Myr curves represent the age after the peak of SF which occurs at  $\simeq 2.5 \times 10^6$  yr and  $\simeq 7 \times 10^6$  yr after the onset of the SF, respectively. For the 100 Myr curve the crosses are in 10 Myr intervals and the first point to the right indicates 100 Myr before the peak of SF.

The interpretation of this figure to derive the ages of the clusters may be somewhat problematic when only a few points are available, because the observations are sometimes located close to several curves. Moreover, for the form of the SF chosen here the 100 Myr curve crosses both the 1 Myr and 5 Myr curves, and a degeneracy between the total duration of the episode of SF and its age may occur. In the case of the brightest stellar clusters in NGC 2903, however, it is clearly seen from the figure that most of the points are well reproduced by the models, and in fact, they lie parallel to the 1 Myr and 5 Myr model outputs. This suggests that short-duration bursts are responsible for the properties of the stellar clusters, rather than constant star formation. The ages measured from the peak of the SF of most of the clusters show a very narrow range, between  $4 \times 10^6$  yr and  $7 \times 10^6$  yr. The observed values for the E and W positions indicate an older population, in good agreement with their location outside the SF ring. The position of the nucleus on this diagram is ambiguous, although it shows values similar to those of the E and W positions. The absolute ages of the knots depend upon the specific form assumed for the SF with ranges  $10 - 14 \times 10^6$  yr and  $6.5 - 9.5 \times 10^6$  yr for the 1 Myr and the 5 Myr models respectively.

### 5.3 Masses

We can also obtain an estimate of the masses of the stellar clusters using evolutionary synthesis models, now in combination with a NIR colour-magnitude diagram. An advantage of using a NIR colour-magnitude diagram is that the effects of extinction are greatly reduced as compared with the optical. In Table 3 we list the  $m_{F160W}$  and  $K'$  aperture photometry, colours and F160W absolute magnitudes for the fifteen brightest clusters. Typical errors in the colours are  $\simeq 0.20$  mag, and are dominated by the uncertainties due to the galaxy background subtraction.

Figure 10 shows the colour-magnitude diagram, where we have plotted the nucleus of NGC 2903 and the fifteen brightest stellar clusters (Table 3). The lines in this diagram are the model outputs from the 1 Myr Gaussian burst normalized to a total mass of  $10^5 M_{\odot}$  (dotted line), and the 5 Myr Gaussian burst normalized to a total mass of  $10^5 M_{\odot}$  (solid line) and of  $5 \times 10^5 M_{\odot}$  (dashed line). The time evolution of the models is shown from 1 (lower left part of the curve) up to  $50 \times 10^6$  yr (lower right part of the curve). The peak of the  $H$ -band absolute magnitude occurs  $\simeq 6.5 \times 10^6$  yr and  $\simeq 8 \times 10^6$  yr after the peak of SF for the 1 Myr and 5 Myr models, respectively. The parameters used for the models are similar to those used to fit the SF properties of Arp 299 and NGC 1614 (see Alonso-Herrero et al. 2000, 2001 for more details). The arrow shows the effects of two magnitudes of visual extinction. Note that for most of the clusters a value of  $A_V \leq 8$  mag (or similarly in the  $H$ -band  $A_H \leq 1.4$  mag) would move the observed points to the loci of the evolution-

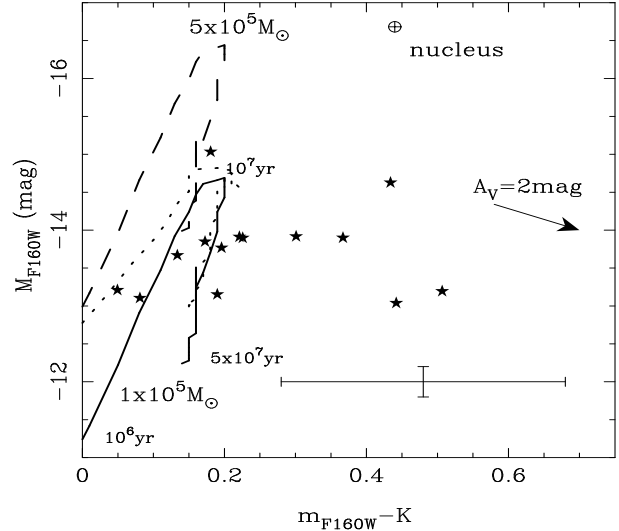


**Figure 10.** Colour-magnitude diagram for the brightest 15 stellar clusters (filled stars, Table 3). We also plot outputs from Rieke et al. (1993) starburst models with Gaussian bursts of SF with FWHM = 1 Myr normalized to a mass of  $10^5 M_{\odot}$  (dotted line), and models with FWHM = 5 Myr normalized to a  $10^5 M_{\odot}$  mass (solid line) and to a  $5 \times 10^5 M_{\odot}$  mass (dashed line). We use a Salpeter IMF. The ages shown next to the solid line model show the evolution from  $10^6$  yr (lower left part of the curve) up to  $50 \times 10^6$  yr after the peak of SF (lower right part of the curve), with the peak of the  $M_{F160W}$  magnitude at around  $8 \times 10^6$  yr.

ary synthesis models. These values of the extinction are consistent with the estimates using the foreground dust screen model in Section 4.

From this figure it is readily seen that all the brightest stellar clusters in NGC 2903 have masses of between  $10^5 M_{\odot}$  and  $5 \times 10^5 M_{\odot}$ , in good agreement with those of Galactic globular clusters (van der Bergh 1995). As noted in Section 3, the extinction estimates obtained from recombination lines and the mixed model are higher than for the foreground dust screen model, which would imply higher masses for the clusters. But because of the lack of spatial correspondence between the stellar clusters and the H II regions we cannot be sure that the high values of the extinction are correct for the stellar clusters. Nevertheless, even if the upper limits to the extinction are used, the masses of the stellar clusters in NGC 2903 are below those of the stellar clusters found in luminous and ultraluminous galaxies (e.g., Alonso-Herrero et al. 2000 and references therein).

We can quantify the contribution of the young stars in the stellar clusters to the total mass in the central region of this galaxy from a statistical point of view. In Section 5.2 we have shown that the ages of the brightest stellar clusters show a very narrow range. Moreover there is no correspondence between the brightness of a knot and its age (Figure 9 and Table 3), that is, the brightest sources do not tend to be the youngest (e.g., knot 3 or knots 2+3). Thus we can assume that the brightnesses of the stellar clusters are proportional to their masses, whereas their age is a second order effect. The evolutionary synthesis models provide the evolution of the  $H$ -band mass-to-light ratio and can be used to derived the masses of the stellar clusters. Evidently, this ratio depends upon the age of the cluster and the form as-

sumed for the SF (and metallicity). From Figure 10 it is clear that this NIR mass-to-light ratio will have a minimum at an age of around  $10^7$  yr (that is, at the peak of the  $H$ -band luminosity). For the range of ages derived for the stellar clusters in NGC 2903 the mass-to-light ratio is uncertain by a 50%. As an illustration of the changes of the infrared mass-to-light ratio as a function of the IMF slope and mass cutoffs, type of star formation and metallicity we refer the reader to figures 51 and 52 in Leitherer et al. (1999) models.

The contribution of the young stellar clusters to the total  $H$ -band luminosity can be obtained by adding the luminosities from the histogram in Figure 8 ( $\simeq 13\%$ ). Now, using the model mass-to-light ratios we find a mass in the young stellar clusters of  $M_{\text{cluster}*} = 2.1 - 3.6 \times 10^8 M_{\odot}$  within the central  $\simeq 625$  pc of NGC 2903. The range in masses takes into account the spread in ages (and thus a varying mass-to-light ratio) of the stellar clusters. For the old stellar population we use the mass-to-light ratio found by Thronson & Greenhouse (1988) and estimate a mass in old stars of  $M_{\text{old}*} = 2.7 \times 10^9 M_{\odot}$  within the same region. The young stellar clusters therefore account for 7 – 12% of the central (625 pc) stellar mass in NGC 2903. Note, however, that a population of even younger stars (see next section), which are ionizing the gas in the bright H II regions, are unaccounted for in the mass calculation.

## 6 STAR FORMATION PROPERTIES

### 6.1 The star-forming regions

As shown in Sections 3 and 4, we have identified eight bright H II regions in the ring of SF of NGC 2903. These H II regions appear resolved with typical sizes of between 16 pc and 50 pc (FWHM). Table 4 lists the observed Pa $\alpha$  fluxes through a 1.2 arcsec-diameter (50 pc) circular aperture, the H $\alpha$  luminosities (corrected for extinction when possible) and the equivalent number of ionizing photons assuming that there are no escaping photons. The extinction corrected H $\alpha$  luminosity of the bright H II region H4 in the ring of SF approaches that of the super-giant H II region 30 Doradus in the LMC ( $\log L(\text{H}\alpha) = 39.8 \text{ erg s}^{-1}$ , Kennicutt, Edgar, & Hodge 1989), but it is below the luminosities of the H II regions in infrared luminous galaxies (Alonso-Herrero et al. 2000, 2001). However, the bright H II regions in the central region of NGC 2903 are of comparable luminosity as the brightest H II regions in nearby spiral galaxies (Kennicutt et al. 1989; Rozas et al. 1996; Knapen 1999).

Although spectroscopic information is not available for the bright H II regions, we can compare the relative values of their EW of Pa $\alpha$  with those of the stellar clusters. A map of the EW of Pa $\alpha$  can be constructed by dividing the continuum-subtracted *HST*/NICMOS Pa $\alpha$  line emission image by the  $H$ -band continuum image. Comparing the relative values of the EW(Pa $\alpha$ ) at the location of the H II regions H1 and H4 with the youngest stellar cluster (4+11), we find that these two H II regions have values of the EW of between three and four times greater than 4+11, indicating ages for these H II regions of less than  $3 \times 10^6$  yr after the peak of SF (for the 1 Myr model). The other H II regions in the ring show values for the EWs similar to that of 4+11, but greater than the other stellar clusters. Again using the

outputs from the evolutionary synthesis models, we find that the number of ionizing photons (Table 4, column 7) of the H II regions implies  $\simeq 10^5 M_{\odot}$  of recently formed stars with ages of  $\simeq 1.5 - 4.5 \times 10^6$  yr after the peak of star formation using the 1 Myr model. In conclusion, the bright H II regions in the star forming ring are younger than the stellar clusters, but with similar stellar masses. This strongly suggests that these H II regions are the progenitors of the stellar clusters.

### 6.2 The SF efficiency

The morphology of the nuclear star forming ring revealed by the *HST*/NICMOS images allows an accurate estimate of the SF efficiency in this galaxy. Using the well-known relation between the SF rate (SFR) and the H $\alpha$  luminosity (e.g., Kennicutt 1998), and the extinction corrected H $\alpha$  luminosity (Table 4), we find  $\text{SFR} = 0.7 M_{\odot} \text{ yr}^{-1}$  in the nuclear ring of NGC 2903. This value corresponds to a SFR surface density of  $\log \Sigma_{\text{SFR}} = 0.37 M_{\odot} \text{ yr}^{-1} \text{ kpc}^{-2}$ . The total mass in molecular gas within the central 770 pc of NGC 2903 has been estimated by Jackson et al. (1991) using CO observations and the standard Galactic CO-to-H $_2$  conversion factor to be  $3 \times 10^8 M_{\odot}$  and the molecular gas density is  $\log \Sigma_{\text{H}_2} = 2.60 M_{\odot} \text{ pc}^{-2}$  (Kennicutt 1998). The use of the standard Galactic CO-to-H $_2$  factor is uncertain in general in external galaxies (e.g., Adler et al. 1992; Rand 1993; Nakai & Kuno 1995), and certainly so in environments like the one under consideration. It is conceivable that SF locally causes an increase in the emission by CO molecules, as cautiously hinted at by, e.g., Adler, Lo, & Allen (1991) and Allen (1992). This would not be accompanied by an increase in the underlying molecular gas mass, as would be expected through the use of a constant ratio. Given the amount of massive SF in the core region of NGC 2903, we may expect the CO measurements there in combination with the use of a standard ratio value to lead to an overestimate of the amount of molecular hydrogen, and thus to an underestimate of the SF efficiency derived from it. In any case, the numbers derived above for  $\log \Sigma_{\text{SFR}}$  and  $\log \Sigma_{\text{H}_2}$  would show that the global SF efficiency in NGC 2903 is significantly higher than for normal galaxies, and it is in fact at the lower end of the relation found for infrared luminous star forming galaxies, which can approach  $\simeq 100\%$  efficiencies over  $10^8$  yr (Kennicutt 1998).

## 7 SUMMARY AND CONCLUSIONS

We have presented high resolution NIR imaging and spectroscopy of the nuclear region of NGC 2903 and conducted a detailed study of its morphology and SF properties. Our main conclusions are:

- The bright infrared hot spots (known from ground-based observations) are resolved into individual stellar clusters or groups of these in our AO and *HST*/NICMOS images.
- The *HST*/NICMOS Pa $\alpha$  (at 1.87  $\mu\text{m}$ ) image reveals a ring of star formation (diameter  $\simeq 625$  pc) with bright H II regions. The overall morphology of the Pa $\alpha$  emission is similar to the 2 cm and 20 cm radio morphologies, which seems to indicate a significant contribution of thermal emission to the total radio emission.

- The high resolution images show a complex distribution of the extinction in the CNR of this galaxy. However the derived values of the extinction are relatively modest (with values of up to  $A_V = 9.5$  mag or infrared extinction at the  $H$ -band of up to  $A_H = 1.6$  mag for a foreground dust screen model).

- We combined spectroscopic and photometric information available for the stellar clusters with evolutionary synthesis models to constrain their SF properties. Short-lived bursts of SF (Gaussian bursts with FWHM = 1, 5 Myr) produced a good fit to the data. The stellar clusters have luminosities similar to the young stellar clusters in the Antennae galaxy. They are relatively young, with a narrow range of ages,  $4 - 7 \times 10^6$  yr after the peak of SF (the absolute ages depend upon the specific duration of the burst of SF), and contribute to some 7 – 12% of the stellar mass in the central regions of NGC 2903.

- The H II regions in the star forming ring exhibit luminosities approaching that of 30 Doradus, and are younger ( $1 - 4 \times 10^6$  yr after the peak of SF) than the stellar clusters.

- The ages and masses derived for the bright stellar clusters and H II regions suggest that the H II regions are the progenitors of the bright infrared clusters. This may offer an explanation for the lack of a detailed spatial correspondence between the clusters and the H II regions.

- Finally, we show that the SF efficiency in the central kpc of NGC 2903 is more elevated than in normal galaxies, similar to (although slightly smaller than) those for infrared luminous galaxies.

## ACKNOWLEDGMENTS

This work is partly based on observations collected at UKIRT. The UKIRT is operated by the Joint Astronomy Centre on behalf of the UK Particle Physics and Astronomy Research Council. Based on observations with the NASA/ESA Hubble Space Telescope, obtained at the Space Telescope Science Institute, which is operated by the Association of Universities for Research in Astronomy, Inc. under NASA contract No. NAS5-26555.

We are grateful to Dr. C. G. Wynn-Williams for providing us with the radio data.

We thank Drs. René Doyon, Dolores Pérez-Ramírez, and Daniel Nadeau for help with the CFHT observations, and Dr. Marianne Takamiya for help with those on UKIRT.

## REFERENCES

Adler D. S., Lo K. Y., Allen, R. J. 1991, *ApJ*, 382, 475  
 Adler D. S., Lo K. Y., Wright M. C. H., Rydbeck G., Plante R. L., Allen R. J. 1992, *ApJ*, 392, 497  
 Allen R. J., 1992, *ApJ*, 399, 573  
 Alonso-Herrero A., Rieke G. H., Rieke M. J., Scoville N. Z. 2000, *ApJ*, 532, 845  
 Alonso-Herrero A., Engelbracht C. W., Rieke M. J., Rieke G. H., Quillen A. C., 2001, *ApJ*, in press (astro-ph/0008317)  
 Barth A. J., Ho L. C., Filippenko A. V., Sargent W. L., 1995, *AJ*, 110, 1009  
 Beck S. C., Beckwith S., Gatley I., 1984, *ApJ*, 279, 563  
 Böker T. et al., 1999, *ApJS*, 124, 95  
 Buta R., Combes F., 1996, *Fund. Cosmic Phys.*, 17, 95  
 Carollo C. M., Stiavelli M., Mack J., 1998, *AJ*, 116, 68

Colina L., Wada K., 2000, *ApJ*, 529, 845  
 de Vaucouleurs G., de Vaucouleurs A., Corwin H. G. Jr., Buta R. J., Paturel G., Furgue P., 1991, *Third Reference Catalogue of Bright Galaxies*. Springer, New York (RC3)  
 Doyon R., Joseph R. D., Wright G. S., 1994, *ApJ*, 421, 101  
 Elmegreen B. G., Elmegreen D. M., Brinks E., Yuan C., Kaufman M., Klaric M., Montenegro L., Struck C., Thomasson M., 1998, *ApJ*, 503, L119  
 Elmegreen D. M., Chromey F. R., Sawyer J. E., Reinfeld E. L. 1999, *AJ*, 118, 777  
 Engelbracht C. W., Rieke M. J., Rieke G. H., Kelly D. M., Achtermann J. M., 1998, *ApJ*, 505, 639  
 Hawarden T. G., Letawsky M. B., Ballantyne D. R., Casali M. M., 2000, *MNRAS*, in preparation  
 Heller C. H., Shlosman I., 1994, *ApJ*, 424, 84  
 Hummer D. G., Storey P. J., 1987, *MNRAS*, 224, 801  
 Jackson J. M., Eckart A., Cameron M., Wild W., Ho P. T. P., 1991, *ApJ*, 375, 105  
 Kennicutt R. C. Jr., Edgar B. K., Hodge P. W., 1989, *ApJ*, 337, 761  
 Kennicutt R. C. Jr., 1998, *ApJ*, 498, 541  
 Knapen J. H., 1999, in *The Evolution of Galaxies on Cosmological Timescales*, ASP Conference Series, eds. J. E. Beckman and T. J. Mahoney, Vol 187, p. 72  
 Knapen J. H., Beckman J. E., Shlosman I., Peletier R. F., Heller C. H., de Jong R. S., 1995a, *ApJ*, 443, L73  
 Knapen J. H., Beckman J. E., Heller C. H., Shlosman I., de Jong R. S., 1995b, *ApJ*, 454, 623  
 Laine S., Knapen J. H., Pérez-Ramírez D., Doyon R., & Nadeau D., 1999, *MNRAS*, 302, 33  
 Leitherer C., Schaerer D., Goldader J. D., González-Delgado R., Robert C., Kune D. F., de Mello D. F., Devost D., Heckman T. M., 1999, *ApJS*, 123, 3  
 Mountain C. M., Robertson D. J., Lee T. J., Wade R., 1990, *Proc. SPIE*, 1235, 25  
 Nakai N., Kuno N., 1995, *PASJ* 47, 761  
 Pérez-Ramírez D., Knapen J. H., Peletier R. F., Laine S., Doyon R., Nadeau D., 2000, *MNRAS*, 317, 234  
 Pérez-Ramírez D., Knapen J. H., 2000, *MNRAS*, submitted  
 Piner B. G., Stone J. M., Teuben P. J., 1995, *ApJ*, 449, 508  
 Planesas P., Colina L., Pérez-Olea D., 1997, *A&A*, 325, 81  
 Puxley P. J., Doyon R., Ward M. J., 1997, *ApJ*, 476, 120  
 Puxley P. J., Brand P. W. J. L., 1999, *ApJ*, 514, 675  
 Quillen A. C., Frogel J. A., González R. A., 1994, *ApJ*, 437, 162  
 Rand R.J. 1993, *ApJ*, 404, 593  
 Regan M. W., Elmegreen D. M., 1997, *AJ*, 114, 965  
 Regan M. W., Sheth K., Vogel S. N., 1999, *ApJ*, 526, 97  
 Rieke G. H., Lebofsky M. J., 1985, *ApJ*, 288, 618  
 Rieke G. H., Loken K., Rieke M. J., Tamblin P., 1993, *ApJ*, 412, 99  
 Rigaut F., et al., 1998, *PASP*, 110, 152  
 Rozas M., Beckman J. E., Knapen J. H., 1996, *A&A*, 307, 735  
 Ryder S. D., Knapen J. H., 1999, *MNRAS*, 302, L7  
 Ryder S. D., Knapen J. H., Takamiya M., 2000, *MNRAS*, submitted  
 Sakamoto K., Okumura S. K., Ishizuki S., Scoville N. Z., 1999, *ApJS*, 124, 403  
 Scoville N. Z., Evans A. S., Thompson R., Rieke M., Hines D. C., Low F. J., Dinshaw N., Surace J. A., Armus L., 2000, *AJ*, 119, 991  
 Shlosman I., Frank J., Begelman M. C. 1989, *Nature*, 338, 45  
 Shlosman I., 1999, in Beckman J. E., Mahoney T. J., eds, *The Evolution of Galaxies on Cosmological Timescales*. Astron. Soc. Pac., San Francisco, Vol. 187, 100  
 Simons D. A., Depoy D. L., Becklin E. E., Capps R. W., Hodapp K.-W., Hall D. N. B., 1988, *ApJ*, 335, 126  
 Surace J. A., Sanders D. B., Vacca W. D., Veilleux S., Mazzarella J. M., 1998, *ApJ*, 492, 116

- Telesco C. M., Harper, D. A., 1980, ApJ, 235, 392  
Thronson H. A., Greenhouse M. A. 1988, ApJ, 327, 671  
van der Bergh S., 1995, Nature, 374, 215  
Vanzi L., Alonso-Herrero A., Rieke G. H. 1998, ApJ, 504, 93  
Whitmore B. C., Zhang Q., Leitherer C., Fall S. M., Schweizer  
F., Miller B. W., 1999, AJ, 118, 1551  
Wynn-Williams C. G., Becklin E. E., 1985, ApJ, 290, 108